

## RESEARCH ARTICLE

# Near-infrared light activated core-shell electrospun nanofibers decorated with photoactive plasmonic nanoparticles for on-demand smart drug delivery applications

Mohammad Ali Haghghat Bayan<sup>1</sup> | Yasmin Juliane Dias<sup>2</sup> | Chiara Rinoldi<sup>1</sup> | Paweł Nakielski<sup>1</sup> | Daniel Rybak<sup>1</sup> | Yen B. Truong<sup>3</sup>  | Alexander L. Yarin<sup>2,4</sup> | Filippo Pierini<sup>1,3</sup> 

<sup>1</sup>Department of Biosystems and Soft Matter, Institute of Fundamental Technological Research, Polish Academy of Sciences, Warsaw, Poland

<sup>2</sup>Department of Mechanical and Industrial Engineering, University of Illinois at Chicago, Chicago, Illinois, USA

<sup>3</sup>Commonwealth Scientific and Industrial Research Organization (CSIRO) Manufacturing, Clayton, Victoria, Australia

<sup>4</sup>School of Mechanical Engineering, Korea University, Seoul, Republic of Korea

## Correspondence

Filippo Pierini, Department of Biosystems and Soft Matter, Institute of Fundamental Technological Research, Polish Academy of Sciences, ul. Pawińskiego 5B, Warsaw 02-106, Poland.

Email: [fpierini@ippt.pan.pl](mailto:fpierini@ippt.pan.pl)

## Funding information

National Science Centre, Grant/Award Number: 2020/38/E/ST5/00456; Polish National Agency for Academic Exchange, Grant/Award Number: BPN/BEK/2021/1/00161; National Agency for Academic Exchange, Grant/Award Number: PPI/APM/2018/1/00045/U/001; Polish Ministry of Science and Higher Education

## Abstract

Over the last few years, traditional drug delivery systems (DDSs) have been transformed into smart DDSs. Recent advancements in biomedical nanotechnology resulted in introducing stimuli-responsiveness to drug vehicles. Nano-platforms can enhance drug release efficacy while reducing the side effects of drugs by taking advantage of the responses to specific internal or external stimuli. In this study, we developed an electrospun nanofibrous photo-responsive DDSs. The photo-responsivity of the platform enables on-demand elevated drug release. Furthermore, it can provide a sustained release profile and prevent burst release and high concentrations of drugs. A coaxial electrospinning setup paired with an electro spraying technique is used to fabricate core-shell PVA-PLGA nanofibers decorated with plasmonic nanoparticles. The fabricated nanofibers have a hydrophilic PVA and Rhodamine-B (RhB) core, while the shell is hydrophobic PLGA decorated with gold nanorods (Au NRs). The presence of plasmonic nanoparticles enables the platform to twice the amount of drug release besides exhibiting a long-term release. Investigations into the photo-responsive release mechanism demonstrate the system's potential as a “smart” drug delivery platform.

## KEYWORDS

electrospun core-shell nanofibers, NIR-light activation, on-demand drug release, plasmonic nanoparticles, stimuli-responsive nanomaterials

This is an open access article under the terms of the [Creative Commons Attribution-NonCommercial](https://creativecommons.org/licenses/by-nc/4.0/) License, which permits use, distribution and reproduction in any medium, provided the original work is properly cited and is not used for commercial purposes.

© 2023 The Authors. *Journal of Polymer Science* published by Wiley Periodicals LLC.

## 1 | INTRODUCTION

The strategy of providing medication or other pharmacological substances to produce a long-lasting therapeutic effect is realized with drug delivery systems (DDSs).<sup>1,2</sup> Scientific discoveries revealed that controlled delivery of drugs could affect treatment efficacy.<sup>3</sup> Hence, DDSs have grown in importance in the pharmacological industry over the past few decades.<sup>4–6</sup> Controlled drug release is one of the methods of drug delivery and an essential topic in biomedical research.<sup>7</sup> In this process, a polymer, ceramic, or metal carrier is combined with a drug or active agent in a designed approach so that an active agent can be released into the human body in a predetermined and desired way.<sup>8</sup> By taking advantage of controlled releasing carriers as DDSs, the drug molecules could be sustainably released. Additionally, the carriers can maintain an effective drug concentration for the designated period.<sup>9</sup> The DDS optimization also avoids burst release reducing the side effects of high concentrations of drugs.<sup>10</sup> An ideal drug carrier should have the following characteristics: stable physical and chemical properties, biocompatibility, extremely low toxicity, and adjustable drug release.<sup>11</sup> In recent years, the research on DDSs has focused on enhancing the carrier's release kinetic, incorporating different techniques to produce new generations of carriers.<sup>12,13</sup> DDSs can efficiently target a specific living tissue and promote drug absorption. Moreover, they can release the drug on demand to achieve an effective and safe therapeutic effect; these novel systems are called stimuli-responsive DDSs or “smart” DDSs (SDDSs).<sup>14–19</sup>

Stimuli-responsive drug carriers can trigger drug release from the nanoplateforms.<sup>20–22</sup> One of the most exciting stimuli responses is the photo-responsiveness of photoactive material. Photoactive materials are chemical compounds in one or more spectrum bands sensitive to electromagnetic radiation. Electromagnetic radiation can cause chemical or physical changes in the material's structure. Among electromagnetic waves, UV and IR are the most used in biomedical applications.<sup>23</sup> UV light can damage tissues and cells due to high scattering and absorption by water and proteins in the human body through a one-photon mechanism. In contrast to UV, near-infrared (NIR) light can be absorbed through a two-photon process. The one-photon absorption of UV light and the two-photon absorption of NIR light supply enough energy to activate the photoreactions of photo-responsive material.<sup>24,25</sup> NIR light has no adverse effects on tissues or cells.<sup>26</sup> It can penetrate tissues up to several centimeters with slim scattering and absorption by water and endogenous proteins. Due to the characteristics mentioned above, the NIR-responsive polymeric SDDSs are promising for on-demand drug administration.<sup>27,28</sup>

Plasmonic nanoparticles can efficiently convert the photons' energy into the energy of charge carriers in nanoparticles.<sup>29</sup> Among plasmonic nanoparticles, gold nanoparticles are of high interest due to their surface functional properties and the ability to generate heat through irradiation. Due to the localized surface plasmon resonance (LSPR) phenomenon, gold nanoparticles strongly absorb light and convert it into thermal energy. Therefore, a specific laser frequency stimulating gold particles can produce a hot zone with a radius a thousand times larger than their size. This effect can be used in various applications. For instance, gold nanoparticles' LSPR can damage cancer cells or bacteria with a process called photothermal therapy (PTT).<sup>30,31</sup> Thus, gold nanorods (Au NRs) are one of the most promising plasmonic PPT agents. The lowest light absorption in most body tissues is in the 700 to 900 nm wavelength band, called the “NIR tissue window.”<sup>32</sup> As a result, using Au NRs, which possess plasmon resonance in this window, reduces the risk of damaging healthy cells.<sup>33,34</sup>

Electrospinning is a straightforward and economical technique for producing micro and nanofibers utilizing polymer solutions by applying an electrical field. Fibers fabricated by this method have large specific volumes, favorable mechanical properties, and extensive contact area, yielding numerous applications for materials produced.<sup>17,35</sup>

Electrospinning can produce sophisticated structures such as hollow, core-shell, or porous nanofibers.<sup>36</sup> Initially introduced in 2003, the coaxial electrospinning method made it possible to fabricate nanofibers from two or more types of polymer solutions with a broader range of morphologies.<sup>37,38</sup> This method aims to create more advanced nanofibers and nanostructures designed to improve the efficiency of targeted applications.<sup>39–41</sup>

Electrospraying is a technique similar to electrospinning but utilizes electrical force to produce nanoparticles instead of nanofibers. In electrospraying, the liquid at the outlet of a nozzle is exposed to electrical Maxwell stresses, pulling the surface normally and against the restraining surface tension effect. The Maxwell stresses arise in the air between the liquid meniscus affected by an inserted electrode or the nozzle being an electrode (at high DC voltage applied) and a grounded counter-electrode. One of the benefits of electrospraying is the ability to fabricate droplets on the micro-nano scale, regarding fabrication parameters.<sup>42,43</sup>

In the present study, we report the fabrication of photo-responsive PVA-PLGA core-shell nanofibers decorated with plasmonic Au NRs using a simultaneous electrospinning-electrospraying method. A coaxial electrospinning setup provided a shell of poly(lactic-co-glycolic acid) (PLGA) over a poly(vinyl alcohol) (PVA) core and a drug model.<sup>44</sup> PVA is a water-soluble

biocompatible polymer without toxicity to cells and is an ideal polymer for fabricating fibrous biomaterials. Therefore, PVA is selected as the core for loading a hydrophilic drug. PLGA is a hydrophobic synthetic polymer with outstanding biocompatibility.<sup>45</sup> Hence, PLGA can provide an efficient protective shell for the water-soluble core of the system. The as-spun fibers can be used as a drug carrier, combining the outstanding properties of both polymers. The present research focuses on designing and optimizing unique stimuli-response material. These materials can control the drug release kinetics on-demand by applying external stimulation. Simultaneous decoration of core-shell nanofibers with Au NRs provided photo-responsive properties to the assembled fibrous material. It is anticipated that the photo-responsive PVA-PLGA nanofibers matrix decorated by Au NRs holds great promise as on-demand drug carriers.

## 2 | RESULTS AND DISCUSSION

### 2.1 | Structure of the core-shell platform

Plasmonic nanoparticle decorated core-shell fibers were designed by coaxial electrospinning of PVA and PLGA solutions with simultaneous electrospaying of Au NRs alcosol. In Figure 1A, the schematic of the electrospinning-coelectrospaying technique is illustrated. The core-shell structure was observed already from the modified Taylor cone of electrospinning, and the fiber morphology was confirmed using TEM. The fiber fabrication with coaxial electrospinning of PVA and PLGA, decoration with electrospaying by Au NRs, and encapsulation of RhB as a drug model inside the polymer core structure were performed simultaneously.

Plasmonic particles on the polymer core-shell fibers provided a well-designed hierarchical structure to the final platform. Due to the presence of Au NRs, fibrous drug carriers can produce heat in response to the NIR light triggering (Figure 1B). For this reason, it was advantageous to employ the photo-response ability of Au NRs to develop SDDs for modulated drug release application. Starting from the principle that the induced temperature can accelerate the drug release kinetics of the core-shell system.

### 2.2 | Morphological characterizations

The schematic in Figure 2A represents the structure of the platform's core consisting of PVA and a shell of PLGA that form the final core-shell structure. Also, the placement of Au NRs is visualized in the schematic. The FE-SEM microscopy was conducted to visualize the presence of Au NRs, confirming the presence of nanoparticles on the fibers (Figure 2B). The in-depth morphology of the produced coaxial PVA-PLGA fiber is shown in the TEM micrograph in Figure 2C. The contrast, created by electron beam diffraction, represents the distinctive phase in the core-shell structure. The bright region represents the fiber's core, and the dark region indicates the shell. The diameters of the core and shell are approximately 634 and 981 nm, respectively.

Figure 2D presents SEM images of PVA, PLGA, and the core-shell fibers. The monolithic fiber fabrication process was optimized to achieve a fibrous structure similar to the core-shell fibers as a control for drug release studies. The associated diameter distribution of fabricated nanofibers reveals the average diameter of PVA nanofibers of  $972 \pm 76$  nm (Figure S1). Similarly, the average thickness of PLGA fibers is  $952 \pm 41$  nm,

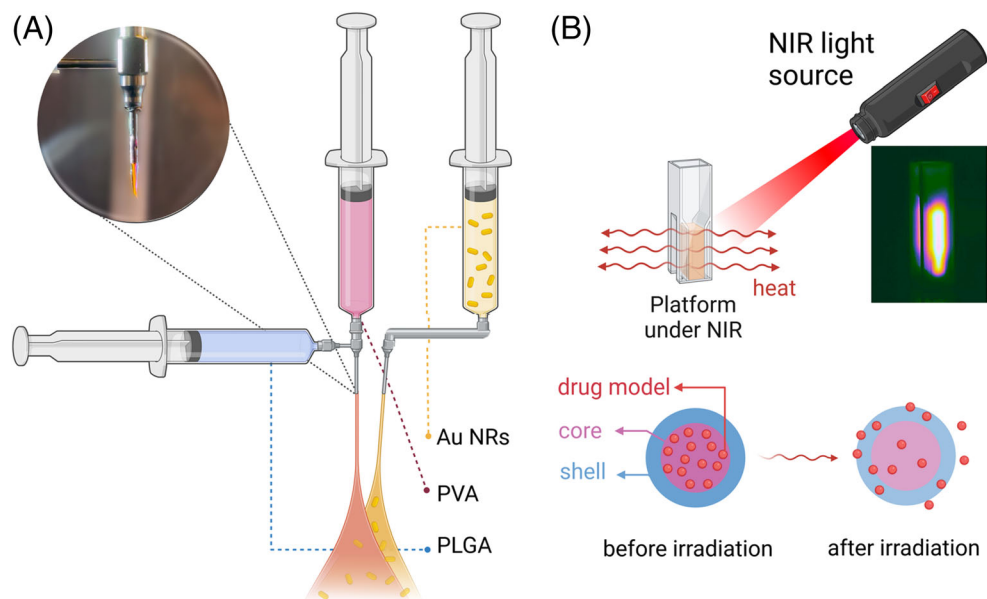


**FIGURE 1** Illustration of material preparation. (A) Schematic presenting the fabrication by coaxial electrospinning of PVA and RhB core and PLGA shell, concurrent with Au NRs electrospaying. (B) Representative scheme of the photo-responsiveness of the fabricated material under the NIR light, highlighting that an increase in temperature can facilitate a drug release process.

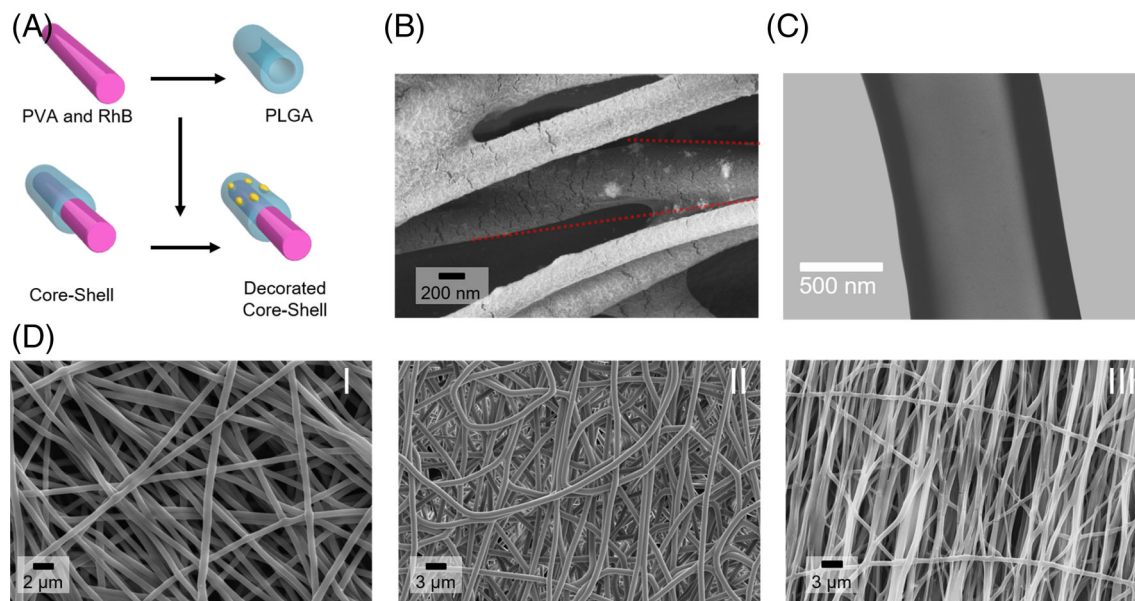


**FIGURE 2** Morphological analysis of the electrospun fibers and the core-shell platform. (A) Schematic drawing representing fabrication of core-shell fibers composed of PVA and RhB core, PLGA shell, and decorated with Au NRs. (B) FE-SEM micrograph of Au NRs on the surface of the core-shell platform. (C) The inner core structure and the outer shell of the fiber are evident in the TEM micrograph of the core-shell platform. (D) SEM images of I- PVA electrospun fibers, II- PLGA monolithic fibers, and III- core-shell fibrous materials, demonstrating similar diameters of the monolithic fibers and the core-shell platform.

and of the core-shell platform,  $993 \pm 33$  nm. The efforts to produce fibers with comparable thickness were undertaken to compare the drug release kinetics of the fibers mutually. Figure S2 reports different magnifications of SEM images of the fabricated fibers, highlighting the defect-free, beadless, and geometrical uniformity of the electrospun nanofibers.

### 2.3 | Physio-chemical characterizations

The ATR-FTIR (Figure 3A) was performed to characterize the chemical structure of the fabricated platform. As can be seen, in both PLGA and core-shell samples, at  $1750\text{ cm}^{-1}$ , there are peaks related to the  $(-\text{CO}-)$  bonds. Also, at the wavenumber of  $1080\text{ cm}^{-1}$ , the peak related to the  $(-\text{C}-\text{O}-\text{C}-)$  group in both PLGA and core-shell transmissions is visible. However, at  $3445\text{ cm}^{-1}$ , the peak of the hydroxyl group is just displayed for PVA fiber. The absence of a hydroxyl group peak in core-shell fibers exhibits the lack of PVA in the platform's outer layer, indicating that the PLGA shell covers the PVA core.<sup>46</sup>

The PVA, PLGA, and core-shell fibers were analyzed using differential scanning calorimetry (DSC). The DSC thermograms represented the characteristic peaks of melting temperature ( $T_m$ ) and glass transition temperature ( $T_g$ ) (Figure 3B). The melting temperature of pure PVA is assigned to a reasonably large and sharp

exothermic peak visible at about  $180.5\text{ }^\circ\text{C}$ . For the core-shell nanofibers—where PLGA is introduced—this peak is shifted to  $174.2\text{ }^\circ\text{C}$ . This gradual shift of the melting temperature to lower values occurs most probably because of the addition of PLGA in the fiber structure.

Thermogravimetric analysis (TGA) was performed to investigate the thermal properties of the PVA, PLGA, and PVA-PLGA core-shell fibers (Figure 3C). Derivative thermogravimetry (DTG) analysis was also carried out on neat PVA and PLGA fibers and the core-shell structure and reported in Figure S3. The PVA fibers presented a multi-step decomposition process with the central peak at  $263\text{ }^\circ\text{C}$  and a second stage at  $414\text{ }^\circ\text{C}$ . The first peak can be related to the release of acetyl groups transferred to acetic acid molecules and subsequent catalytic degradation of the main chain by in situ chains strapping at a higher temperature.<sup>47</sup> For the neat PLGA fibers, the TGA curve shows that the degradation starts at  $245\text{ }^\circ\text{C}$  and finishes at  $360\text{ }^\circ\text{C}$  with nearly 100% weight loss. The core-shell fiber's TGA curve showed that a shift had occurred at  $320\text{ }^\circ\text{C}$ . This peak provides additional evidence of the presence of PVA in the core-shell. The formation of the core-shell structure was evident when appropriate conditions were met during the platform fabrication.

The photo-responsivity of PVA-PLGA core-shell nanofibers results from the decoration of the fiber surface with Au NRs. The XRD pattern study was carried out to demonstrate the presence of Au NRs in the core-shell

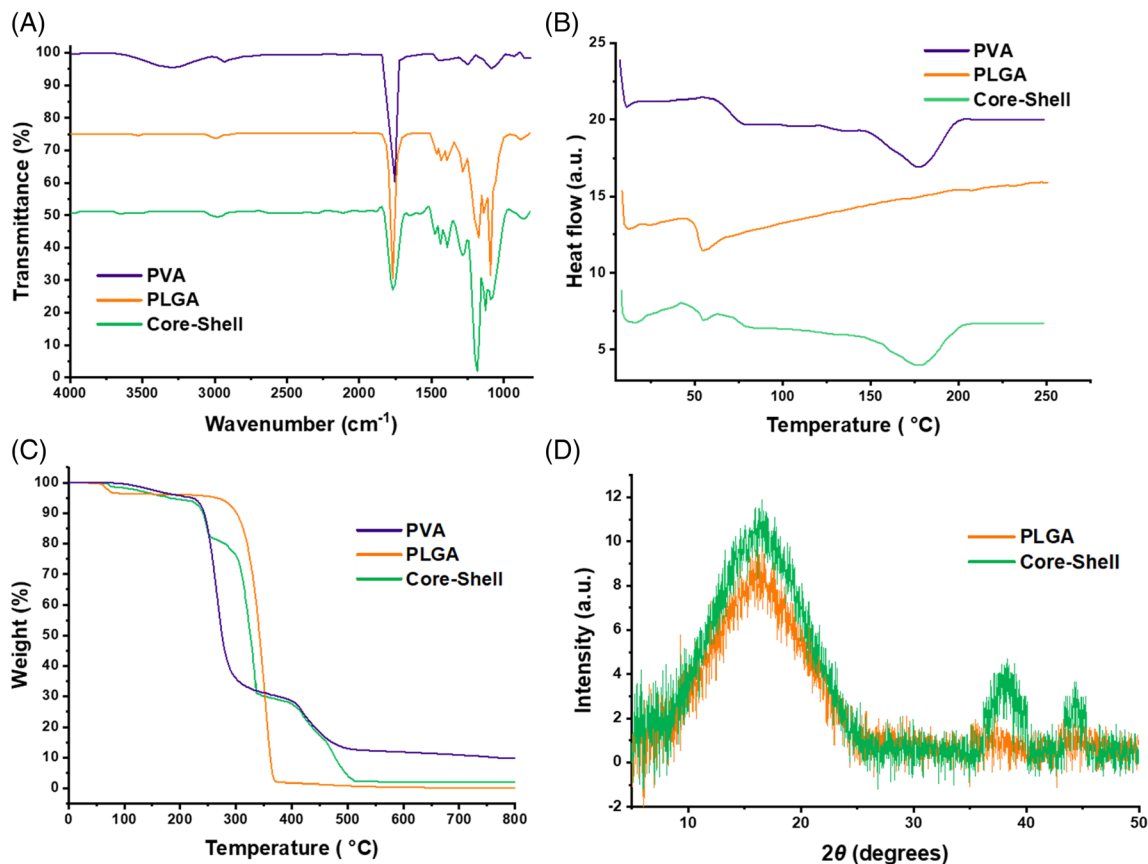


**FIGURE 3** Chemical and physical properties of PLGA, PVA, and core-shell fibers. (A) ATR-FTIR spectra of PLGA and PVA fibers compared with the core-shell platform. (B) DSC graph of the core-shell system, showing the presence of both PVA and PLGA in the structure. (C) Weight percentage versus temperature TGA curves of monolithic fibers along with the core-shell platform. (D) XRD pattern of PLGA fiber compared with core-shell fibers decorated with Au NRs.

fibers (Figure 3D). XRD data revealed the characteristic peaks of Au NRs at  $2\theta$  scattered angles of  $38.0$  and  $44.2^\circ$ , which certifies the presence of Au NRs in the platform.<sup>48</sup>

## 2.4 | Cell studies

In order to verify the biocompatibility of the proposed electrospun substrates and their potential use for biomedical applications, L929 fibroblasts were seeded and cultured onto the fibrous constructs, as also reported in previous studies.<sup>49,50</sup> The presence of a PVA core in the PLGA-based core-shell fibers was investigated in terms of cell response and compared to PLGA pristine fibers and TCP controls. More specifically, cell-materials interactions were evaluated with regard to cell viability, proliferation, and morphology. A Live/Dead assay kit was used to stain the cells seeded onto the constructs and mark them in green or red color according to their live or dead state. Representative Live/Dead images showed a large majority of viable

green cells on both days 1 and 3 of culture (Figure S4), demonstrating the high viability percentage of cells cultured on the proposed substrates ( $>87\%$ , Figure 4A) and the cytocompatibility of the materials. No significant difference was detected among the selected conditions at any time point.

The cell proliferation is reported in Figure 4B, displaying the linear growth of cells during the culture time (1, 3, and 7 days) for all tested conditions. No evident difference between the fibrous samples was detected, while cells seeded onto tissue culture substrates showed a more significant proliferation at the initial stage of the culture (1 and 3 days). This is not surprising since TCPs are treated to be highly cell-friendly, promoting easy and efficient cell adhesion and growth. At the latest stage of culture (day 7), all the tested samples showed similar performance, proving the biocompatibility and suitability of the fibrous substrates for cell viability, activities, and proliferation.

Finally, cell morphological analysis was carried out by observing confocal images of Actin/DAPI stained

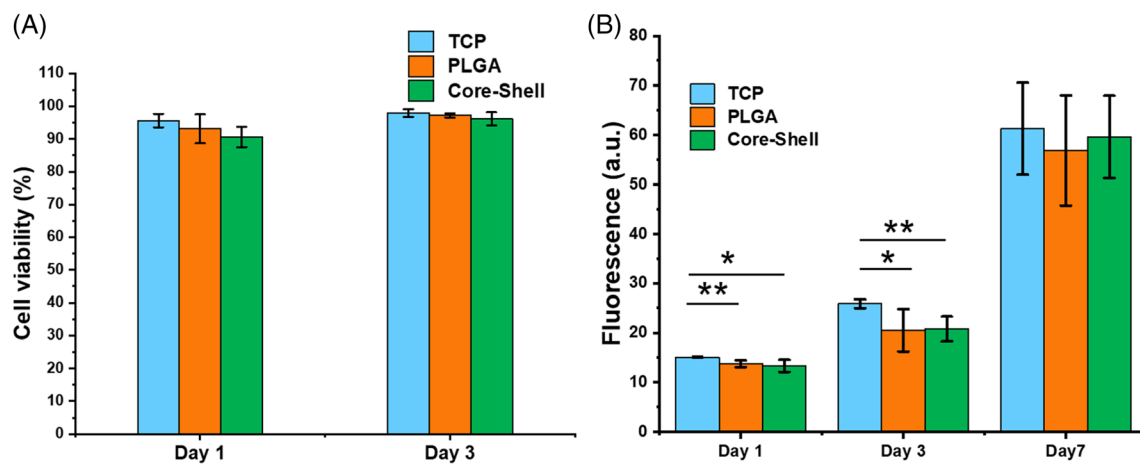


**FIGURE 4** Cell viability of L929 fibroblasts seeded on PVA-PLGA core-shell fibers, PLGA fibers, and TCP. (A) Cell viability percentage calculated from Live/Dead images analysis, reporting cell viability >87% at days 1 and 3 of culture. (B) Cell proliferation up to 7 days of culture, showing the increasing trend during the culture time for all tested samples. Significant differences are reported as \* $p < 0.05$ , \*\* $p < 0.01$ .

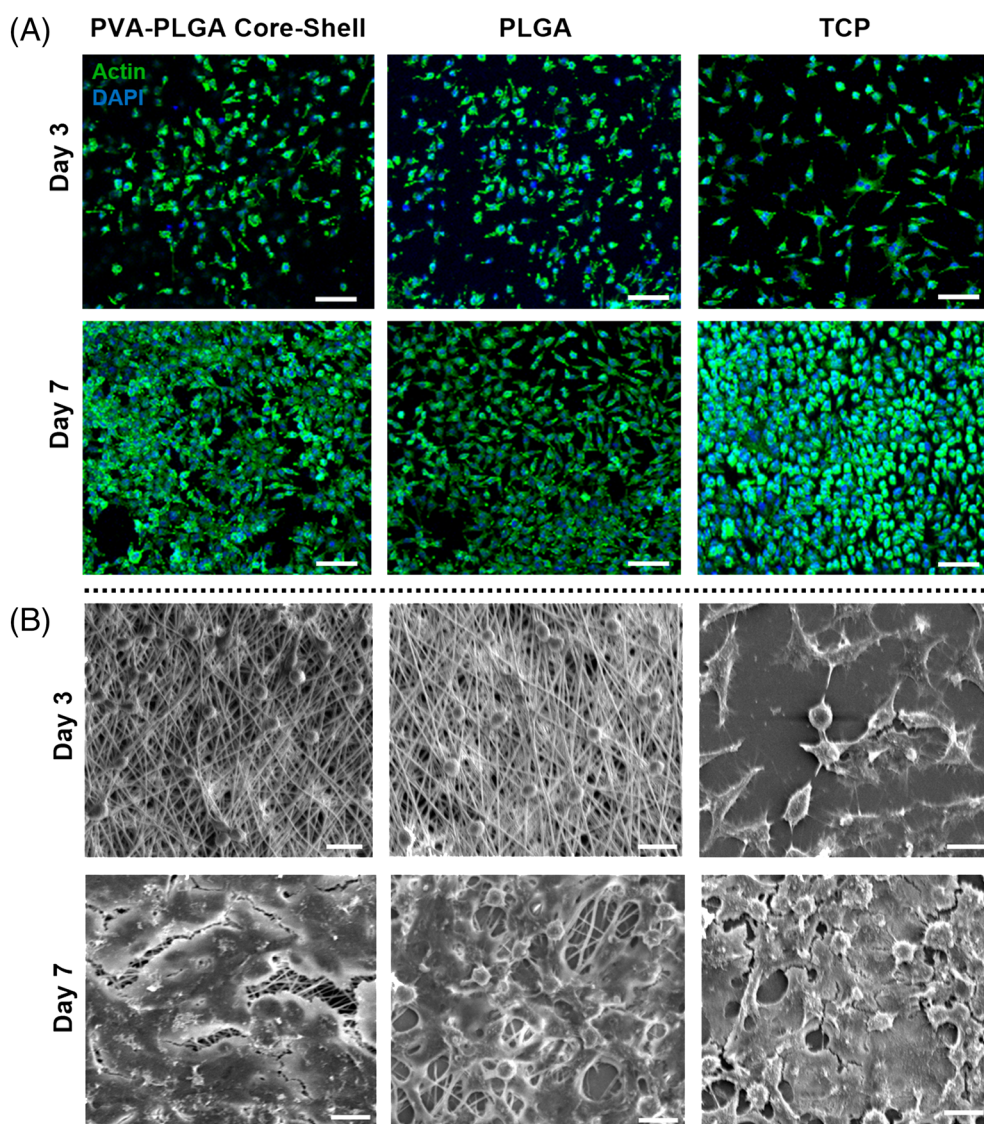


**FIGURE 5** Cell morphology of L929 fibroblasts seeded on PVA-PLGA core-shell fibers, PLGA fibers, and TCP after 3 and 7 days of culture. (A) Cell cytoskeleton is stained green while nuclei are marked in blue (Actin/DAPI staining). Scale bar: 100  $\mu\text{m}$ . (B) SEM images of the cells seeded on fibrous constructs versus TCP control. Scale bar: 20  $\mu\text{m}$ . Data revealed the spreading and elongation of the cells during the culture time.

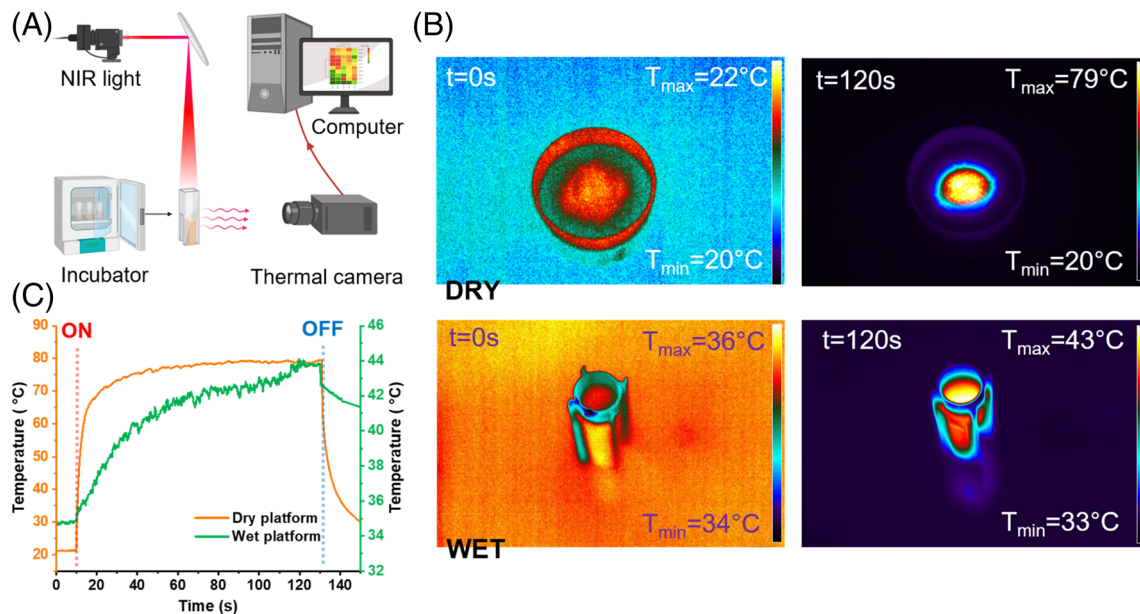


**FIGURE 6** The photo-responsive platform features the fast and on-demand responsiveness of the fabricated material. (A) The schematic of the experimental setup illustrates a thermal camera capturing the temperature of the samples taken out from an incubator and irradiated by a NIR laser. (B) The IR thermogram images of the dry and wet platforms before and after 2 min of irradiation were captured with a thermal camera. Wet samples were analyzed on a hot plate to maintain the platform's temperature at around 37 °C. (C) Temporal plots of the platform's behaviors under the NIR illustration for wet and dry samples, showing the photo-response property of the material.

samples (Figure 5A) and SEM micrographs of the structures (Figure 5B) at days 3 and 7 of culture. At the early stage, the cell cytoskeleton appeared roundish and spherical on the fibrous samples compared to TCP control, most probably due to the lack of cell binding sites in the synthetic polymers. However, during the culture time, cells spread and became more elongated with the typical spindle shape, highlighting the efficient support for cell adhesion and spreading.

## 2.5 | Thermal-response characterizations

The nanofibrous system was decorated with the Au NRs and loaded by Rhodamine-B. The decoration of the platform with plasmonic nanoparticles provided a robust absorption of NIR light that can provide heat due to the outstanding photo-response efficiency.<sup>29</sup> The photo responsiveness to the irradiation of NIR light was confirmed using a thermal camera. The applied NIR laser power was fixed at 2.4 W cm<sup>-2</sup> and irradiated directly on the system with an 808 nm wavelength.

Figure 6A shows a schematic of a NIR laser emitting beam irradiation on the platform (contained in a water-filled vial) and the experimental setup used to investigate the fiber's photothermal activity. Simultaneously with the illumination of samples, the thermal camera records

the thermographic images of the photo-response of the irradiated samples.

Low-power lasers are common in clinical practice due to their bio-stimulating effect in treatment. A lower-power laser, however, results in less heat during the procedure. The heat produced by the SDDSs may not be enough to modulate the drug release if there is a considerable distance between the heat producer (in this case, NIR) and the stimuli-responsive material. The designated strategy was to locate the Au NRs on the surface of the nanofibers instead of putting them inside the core-shell system. The rods are either trapped between the fibers or deposited on their surface. The advantage of this method is the higher generated temperature compared to the particles inside the fibers and the reduction of side effects as the thermally-accelerated polymer matrix degradation.

As can be seen in Figure S5, the location of nanorods can improve the amount of induced heat for dry samples up to 9.6 °C in 2 min. Table S1 displays the temperature responses due to different structures and localization of Au NRs.

The PVA-PLGA core-shell fibers decorated with Au NRs show a strong NIR light absorption and conversion to thermal energy. Figure 6B shows the thermographic images of the platform in dry and wet states. The platform was studied first in the dry state to indicate the maximal potential of the response of the core-shell fiber to NIR light. Subsequently, they were analyzed in water

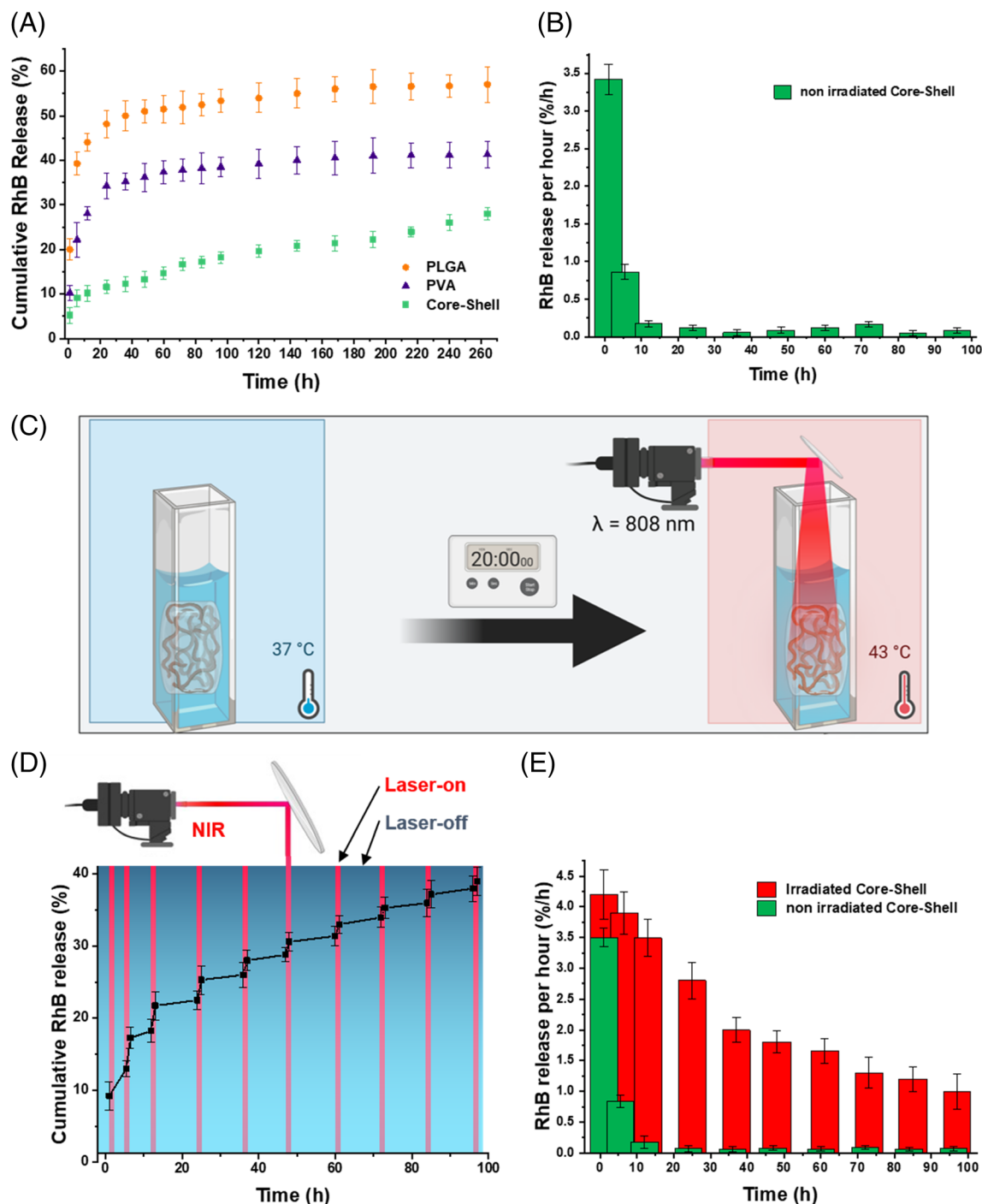


**FIGURE 7** Drug delivery property of the core-shell platform. (A) Cumulative RhB release of three samples of monolith PLGA and PVA and non-irradiated core-shell, showing the burst release of the monolithic fibers. (B) Bar chart of non-irradiated core-shell RhB release per hour, demonstrating the release kinetic of non-irradiated platforms in different time stages. (C) The scheme represents the platform's induced temperature under NIR irradiation, helping to elevate the RhB release. (D) Cumulative RhB release after 10 NIR-light irradiation cycles. The red vertical lines represent a cycle of irradiation. (E) The bar graph of RhB release per hour while the platform was irradiated with NIR light for sequences of 20 min. The graph clearly shows the induced release of RhB upon the laser trigger, assisting the photo response behavior of the fabricated platform.

to reveal the applicable property of the platform for the drug delivery application. The fiber's temperature increased significantly and rapidly, increasing the surrounding water temperature. The highest temperature of

samples was 80 °C for dry samples and 44 °C for fibers in water. (Figure 6C). The plasmonic system was successfully designed to achieve the targeted temperature that triggered the core-shell structure to modulate the drug

release and reach the typical temperature range for performing PTT.

## 2.6 | Drug release studies

This study aimed to develop a smart drug carrier to sustain the drug level in a therapeutic window by exploiting its photo-responsive properties. Sustained drug release can improve therapeutic consequences by reducing drug toxicity and dosing frequency while increasing efficiency. For this purpose, RhB, as a fluorescent dye, was selected as a drug model. Previous studies have demonstrated that developing core-shell structured nanofibers can reduce burst release and sustain long-term drug release.<sup>51</sup>

In Figure 7A, the drug release from PLGA, cross-linked PVA, and core-shell fibers were measured at 37 °C and not triggered by NIR light. The PVA fibers for this study were crosslinked since the monolith PVA can dissolve in water and are incomparable with PLGA and core-shell fibers. To emphasize the effect of morphology on drug release and avoid the dimension effect, the three mentioned fibers were produced with similar fiber size distributions. Considerable differences were observed for two different structures of monolithic and core-shell materials. The RhB release from the monolithic PLGA fibers exhibited an initial burst release. Similarly, in the case of the PVA, RhB was released burst in the early stages of the study. However, the release profile was sustained for core-shell fibers with near first-order release kinetics. As a result of the internal structure, the overall release rate of core-shell fibers was significantly slower, and the release trend constantly increased during the incubation time (Figure 7B). For the monolith fibers, the cumulative release did not increase after 4 days of the study.

The NIR irradiation process is illustrated in Figure 7C. This figure shows the increase in the platform temperature using a  $\lambda = 808$  nm source of NIR. The platform reached 43 °C as a response to irradiating by laser. The RhB release from the irradiated platform utilizing NIR light is visible in Figure 7D. The duration of each irradiation sequence was 20 min. For samples not triggered with NIR light, a small amount of drug release was observed from the nanofibers, indicating that the Au nanorods played a vital role as a nanoscale heat-generating source. These findings appeared promising for biomedical applications that target a modulated drug release. The drug release intensity was elevated upon NIR irradiation after each timepoint of drug release measurement, and the release data were collected before and after each cycle. Figure 7E shows the on-demand release from the core-shell system with Au NRs. The structure of the core-shell fibrous materials led to a regulated and steady release compared to the monolithic

counterparts. Introducing Au nanorods led to the fabrication of a photo-responsive polymer core-shell system to solve this problem. Taking advantage of the stimuli-responsive drug carrier, upon the NIR irradiation, the release kinetic of the vehicle is elevated in response to NIR light irradiation. At the first time point, the release from the core-shell fibers triggered by NIR is about 1.8 folds higher than the non-irradiated core-shell. The platform's exposure to NIR provided 39% of RhB release in the first 96 h of the study, while for the irradiation control sample, the release rate was 18%. The reported results imply the increase in RhB release from the core-shell fiber upon NIR irradiation that is associated with an increase in the temperature of the platform.

The mechanism of RhB release from electrospun nanofibers is based on the drug model's desorption from the nanofibers and its subsequent diffusion in water through the porous structure of the platform. Desorption is the limiting factor in drug release from nanofibers because dye diffusion in water occurs quicker than desorption. The temperature rise caused by the laser irradiation on the platform generates an increase in the kinetics of both desorption and diffusion.

The SEM images of fibers before and after submerging in water were acquired to study the platform's stability. In Figure S6 the SEM micrographs of electrospun platform after submerging in water are collected every 24 h time-points. This figure exhibited the platform will not dissolve in water during the drug release process. Moreover, UV-vis spectroscopy was carried out to observe the effect of drug release and irradiation on the nanorod's detachment. The absorption spectra of samples before and after the irradiation were compared to Au NRs spectra to trace similarities. The spectra of platform media before and after NIR irradiation did not exhibit characteristic peaks of Au NRs at 514 and 808 nm. This result reveals the stability of the nanostructured platform by submerging it in water and even after irradiation (Figure S7). Accordingly, implementing plasmonic nanoparticles, which can be triggered upon a source of light (NIR), is a promising candidate for on-demand release applications. Consequently, the core-shell morphology is suitable for a steady and controlled drug release in the long term.

## 3 | CONCLUSION

The present work described the successful fabrication of a core-shell platform for smart drug delivery. This platform incorporated PVA and PLGA as biocompatible polymers, Rhodamine-B as the drug model, and gold nanorods as plasmonic agents to induce an on-demand platform response upon NIR irradiation.

Core-shell platform was fabricated by coaxial electrospinning of PLGA and PVA paired with electrospinning of Au NRs under controlled environmental conditions. The role of the PLGA shell is crucial for the platform because the PVA core can dissolve in water. Furthermore, the PLGA shell can protect the core from structural damage. In addition, the core-shell structure was proved to be biocompatible and provided sustained drug release kinetics. Moreover, the drug release from the core-shell nanofibrous material was performed under the NIR laser to demonstrate the on-demand performance of the “smart” drug delivery system. The RhB release of the activated platform by NIR light, compared to the non-irradiated system, exhibited successful elevation of the release resulting from response to the stimuli. Moreover, the nanostructured core-shell platform exhibited stability in the structure before and after irradiation with NIR light. The present work highlights that employing plasmonic nanoparticles elevates on-demand the release rate of the drug by increasing the temperature of the platform. The smart fabricated drug delivery system will be helpful in future clinical applications, emphasizing the photoactive feature of this platform.

## 4 | EXPERIMENTAL SECTION

### 4.1 | Materials

For the fabrication of the platform, Polyvinyl alcohol (PVA, 85,000–124,000 Da), Hydrochloric acid (HCl, 37%), Hexafluoro isopropanol (HFIP, 99.5%), acetone (99.5%), and Rhodamine B (RhB, 95%) were purchased from Sigma Aldrich. Poly (D, L-lactide-co-glycolide) (PLGA, Purasorb PDLG 5010) was obtained from Corbion Purac, and gold nanorods (Au NRs,  $\lambda = 800$  nm, OD = 50,  $C = 0.88$  mg mL<sup>-1</sup>) from nanoComposix, USA. For the cell studies, Bovine serum albumin (BSA), hexamethyldisilane (HMDS) and phosphate buffer saline (PBS), glutaraldehyde (GTA), Triton X, DAPI, and L929 murine fibroblasts were bought from Sigma-Aldrich, Poland. “Dulbecco's modified” Eagle's medium (DMEM), fetal bovine serum (FBS), penicillin streptomycin (PS), and EDTA-trypsin were purchased from Gibco Invitrogen, USA. Alexa Fluor 488 Phalloidin and Live/Dead assay were obtained from Thermo-Fisher Scientific, USA.

### 4.2 | Platform preparation

The core polymer solution was prepared by dissolving 1.0 g of PVA in 10.0 mL of DI water, and the fibers' shell solution contained 11 wt% of PLGA in 10.0 mL HFIP.

Furthermore, alcosol of Au NRs was prepared by dissolving 20  $\mu$ L of 50 OD Au NRs (17.6  $\mu$ g) in 100  $\mu$ L of 1:1 ethanol and water solution (v:v). For the coaxial electrospinning setup, the spinneret consisted of a 21G needle for the core and a 16G needle for the shell solution. Core-shell fibers were electrospun by applying 12 kV voltage and a flow rate of 250  $\mu$ L h<sup>-1</sup> for the core solution and 650  $\mu$ L h<sup>-1</sup> for the shell solution. Fibers were collected on a grounded drum rotating at 450 rpm with an 18 cm needle-to-collector distance. The ambient parameters as temperature and humidity in electrospinning were 20 °C and 45%, respectively. Core-shell fibrous materials containing a drug model were fabricated using the same procedure by dissolving 5 mg of RhB in 5 mL of the core solution during the early stage of preparation. In addition, PVA and PLGA monolith nanofibers with similar structural features (e.g., fiber diameter, mat porosity, and thickness) and the same amount of RhB were prepared as control samples. To prepare monolith fibers of PLGA, a solution of 0.9 wt% RhB in shell solution was prepared. The electrospinning parameters for PLGA solution were using a 26G needle, 15 kV was the applied voltage, 800  $\mu$ L h<sup>-1</sup> was the flow rate, with a needle tip to rotor collector distance of 18 cm at a rotation speed rate of 450 rpm. The as-prepared PVA solution was processed with a 26G needle, applying 10 kV voltage, with a flow rate of 400  $\mu$ L h<sup>-1</sup> and similar drum collector parameters used to prepare the PLGA nanofibers. The ambient parameters for PVA electrospinning were 20 °C and 40% relative humidity. After the electrospinning procedure, the PVA fibers were soaked in a 10 mL solution of 2.5 wt% glutaraldehyde in acetone at 44 °C. The next step was adding 100  $\mu$ L of HCl to the crosslinking solution and maintaining the fibers in the solution for 1 h. Finally, the electrospun mat was washed twice with acetone and water. For electrospinning of Au NRs, the prepared alcosol was transferred to a 1 mL syringe equipped with a 26G needle. Electrospinning parameters were set at 12 kV positive voltage, 400  $\mu$ L h<sup>-1</sup> flow rate, needle-collector distance of 18 cm, 450 rpm of drum rotation, at a temperature of 20 °C, and humidity of 45%.

### 4.3 | Morphological characterizations

In order to study the morphology and dimension of the fabricated core-shell nanofibers, transmission electron microscopy (TEM) was performed. For the analysis of the core-shell fibers, electrospinning was performed directly on a TEM grid. The FE-SEM microscopy method was performed to show the presence of Au NRs on the surface of the platform. FE-SEM and TEM studies were conducted using FEI Nova NanoSEM 450 microscope at a working distance of 2 mm and accelerating voltage of

30 kV. Scanning electron microscopy (SEM) observations were performed using JEOL JSM-6390LV at a working distance of 10 mm and 10 kV accelerating voltage to investigate the structure of the monolith fibers. Before the SEM, materials were sputtered with approximately 5 nm thick layers of gold using an SC7620 Polaron mini sputter coater (Quorum Technologies Ltd., Ashford, UK).

#### 4.4 | Chemical characterizations

ATR-FTIR spectroscopy was employed to characterize the presence of the material's functional groups. A Bruker Vertex70 FT-IR Spectrometer measured the transmittance of the material in the wavenumbers range of 4000–400  $\text{cm}^{-1}$  with a resolution of 2  $\text{cm}^{-1}$  and eight scans for each sample. Using Bragg-Brentano geometry, XRD measurements were completed with a Bruker D8 Discover diffractometer in the reflection mode. The analysis was conducted in the angular range (2 thetas,  $2\theta$ ) between 5 and 50°. Data were collected with a step of 0.02° per second at each point. Moreover, XRD made it possible to confirm the presence of Au NRs in the platform. Ultraviolet–visible (UV–Vis) spectra were acquired using a Multiskan GO spectrophotometer (Thermo Scientific, USA) to scan over a range of 400 to 1000 nm with a step of 5 nm. In order to prove the absence of gold nanoparticles in the drug release solution and detect any potential nanoparticle leak caused by laser irradiation, UV–vis spectra were performed.

#### 4.5 | Thermal characterizations

DSC analysis was performed with a Perkin Elmer PYRIS-1, and data were analyzed using OriginPro software. Measurements were performed from 0 to 250 °C, with a rate of 10 °C  $\text{min}^{-1}$  and the weight of the samples were approximately 20 mg. The thermogravimetric analysis (TGA) was performed by a Q5000 (TA Instruments) under the nitrogen purge. The analysis was conducted in the temperature range of 20–800 °C with a heating ramp of 10 °C  $\text{min}^{-1}$ .

#### 4.6 | In vitro cell studies

L929 murine fibroblasts were cultured in DMEM modified with 10% FBS and 1% PS and incubated at 37 °C and 5%  $\text{CO}_2$  until reaching ~80% confluence. The culture medium was changed every other day. During the seeding process, cells were detached by PBS washing and subsequent incubation in 0.05% EDTA-trypsin for

3 min at 37 °C and 5%  $\text{CO}_2$ . The harvested cells were centrifuged for 5 min at 1200 rpm, and the resulting cell pellet was resuspended in a suitable volume of culture medium to obtain the desired cell density in the seeding solution.

PVA-PLGA core-shell and PLGA fibers were electrospun onto coverslips with a diameter of 1.5 cm, sterilized under UV light for 30 min on both sides, and finally placed in 24-well plates. A tissue culture plate (TCP) was tested as a control condition. L929 fibroblasts were seeded on the samples with a cell density of  $10^4$  units  $\text{cm}^{-2}$  and cultured for up to 7 days.

Cells were stained using a Live/Dead assay kit to investigate the viability of L929 fibroblasts seeded on the samples. On days 1 and 3 of culture, the samples were washed with PBS and treated with the Live/Dead staining solution composed of 0.5  $\mu\text{L}$  of calcein (for staining the viable cells in green color) and 2  $\mu\text{L}$  of ethidium homodimer (for red staining of dead cells) in 1 mL of PBS. Three replicates of each sample were soaked in the staining solution and incubated for 10 min at 37 °C and 5%  $\text{CO}_2$ . Then, scaffolds were washed three times in PBS and imaged using a confocal microscope (Leica). Percentages of viable cells were counted using the Cell Counter plugin of ImageJ (National Institute of Health, USA).

The cell proliferation rate was assessed with PrestoBlue assay. Cells seeded on PVA-PLGA core-shell fibers, PLGA fibers, and TCPs were incubated for 1 h in 10% (v/v) PrestoBlue solution in a culture medium at 37 °C and 5%  $\text{CO}_2$ . Five replicates per each condition were tested after 1, 3, and 7 days of culture. The resulting solution was aliquoted in 100  $\mu\text{L}$  aliquots, transferred to a 96-well plate, and analyzed with a fluorometer (Fluoroskan Ascent TM Microplate Fluorometer, Thermo Scientific) with excitation at 530 nm and emission at 620 nm.

The cell morphology was observed in confocal and SEM images of three sample replicates fixed after 3 and 7 days of culture. For the staining of cell cytoskeleton and nuclei, samples were washed with PBS and fixed in 4% paraformaldehyde for 15 min at room temperature. After washing, samples were first incubated in 0.3% (v/v) Triton X-100 solution for 15 min and then in 1% (w/v) BSA for 30 min. Subsequently, samples were treated with a solution of 1:40 Alexa Fluor 488 Phalloidin in PBS in the darkness for 40 min. Finally, cell nuclei were stained using a solution of 1:500 DAPI in PBS for 10 min. Samples were washed and imaged using a confocal microscope (Leica).

For SEM images, the constructs were washed in PBS and fixed in 3% ice-cold GTA for 3 hours. The substrates were then washed three times with deionized water and dehydrated in 50%, 70%, 90%, and 100% concentrated

ethanol solutions for 15 minutes each. Finally, samples were treated with HMDS and dried under a fume hood overnight.

#### 4.7 | Photo-responsivity characterization

The NIR light source was a diode laser (EKSMA OPTICS) operating at 808 nm in the high absorption range of Au NRs (longitudinal plasmon band) with a rectangular profile. A high-resolution thermal camera (FLIR, A655sc) was employed to map and identify the spatial heating distribution and temperature profile under laser illumination. The camera produces thermal images of 640 by 480 pixels with an accuracy of  $\pm 0.2$  °C. It works seamlessly with proprietary software (FLIR ResearchIR Max) to record and process the thermal data acquired by the camera.

#### 4.8 | Drug-release analysis

The release of Rhodamine B from the monolith fibers of PLGA, PVA, and core-shell was analyzed at 37 °C. Circular electrospun mat samples with a diameter of 2 cm and containing approximately 50  $\mu\text{g}$  of dye (Rhodamine-B) were immersed in 1 mL of PBS solution at 37 °C. The vial was sealed and wrapped with aluminum foil to prevent water evaporation and light exposure. The supernatant fluid was exchanged with fresh water and maintained at the incubator to maintain the same temperature as set for any specific test after 1, 4, 10, and 12 h of release. The sample temperature was checked by a FLIR thermal camera several times for each sample. Over the next 4 days, the release level of RhB was measured every 12 h. Subsequently, the measurement time points were reduced to once per day (over the following 7 days). Fluorescence signals were measured with a fluorometer (Fluoroskan Ascent TM Microplate Fluorometer, Thermo Scientific, USA) (excitation-emission 530–620 nm) and used to evaluate the concentration of released RhB based on a calibration curve.

The gold nanorods decorated systems release experiments were carried out using an 808 nm diode laser (EKSMA OPTICS) and a power density of 2400  $\text{mW cm}^{-2}$ . The 1 cm circular decorated core-shell fibers were suspended in a vial filled with 1 mL of deionized water. The vial was additionally secured with a parafilm seal to protect the sample from water evaporation. The samples were irradiated with a NIR laser in periodic cycles of the ON/OFF mechanism of irradiation, and the duration of irradiation was 20 min, and they rested for 40 min for each sequence. Afterward, the supernatant was collected, and its concentration was measured using the fluorometer to evaluate the amount of RhB released.

#### 4.9 | Statistical analysis

Data are presented as mean values  $\pm$  SD. One-way ANOVA test was carried out, and differences were considered statistically significant when the  $p$ -value was  $\leq 0.05$ : \* $p \leq 0.05$ , \*\* $p \leq 0.01$ , \*\*\* $p \leq 0.001$ , \*\*\*\* $p \leq 0.0001$ . Drug release measurements were performed six times for each platform.

#### ACKNOWLEDGMENTS

This work was supported by the National Science Centre (NCN) SONATA BIS Project No. 2020/38/E/ST5/00456 and the Polish National Agency for Academic Exchange (NAWA) under Bekker NAWA Programme, grant number: BPN/BEK/2021/1/00161. The Authors are grateful for the support provided by the National Agency for Academic Exchange (NAWA) grant no. PPI/APM/2018/1/00045/U/001. Figures 1, 6A, 7C, and S7a were created with Biorender; Figure 7D was partially created with Biorender. C.R., P.N., and F.P. acknowledge the financial support from the Polish Ministry of Science and Higher Education through scholarships for outstanding young scientists.

#### ORCID

Yen B. Truong  <https://orcid.org/0000-0003-2210-2414>

Filippo Pierini  <https://orcid.org/0000-0002-6526-4141>

#### REFERENCES

- [1] A. Luraghi, F. Peri, L. Moroni, *J. Controlled Release* **2021**, 334, 463.
- [2] T. Sahu, Y. K. Ratre, S. Chauhan, L. V. K. S. Bhaskar, M. P. Nair, H. K. Verma, *J. Drug Deliv. Sci. Technol.* **2021**, 63, 102487.
- [3] C. Li, J. Wang, Y. Wang, H. Gao, G. Wei, Y. Huang, H. Yu, Y. Gan, Y. Wang, L. Mei, H. Chen, H. Hu, Z. Zhang, Y. Jin, *Acta Pharm. Sin. B* **2019**, 9, 1145.
- [4] D. Steinberg, M. Friedman, *Periodontol 2000* **2020**, 84, 176.
- [5] O. Veiseh, J. W. Gunn, M. Zhang, *Adv. Drug Deliv. Rev.* **2010**, 62, 284.
- [6] S. S. Silva, J. M. Gomes, R. L. Reis, S. C. Kundu, *ACS Appl. Bio Mater.* **2021**, 4, 4000.
- [7] Y. Xu, C. S. Kim, D. M. Saylor, D. Koo, *J. Biomed. Mater. Res. B Appl. Biomater.* **2017**, 105, 1692.
- [8] D. Mishra, J. R. Hubenak, A. B. Mathur, *J. Biomed. Mater. Res. A* **2013**, 101, 3646.
- [9] N. Kamaly, B. Yameen, J. Wu, O. C. Farokhzad, *Chem. Rev.* **2016**, 116, 2602.
- [10] K. S. Butler, P. N. Durfee, C. Theron, C. E. Ashley, E. C. Carnes, C. J. Brinker, *Small* **2016**, 12, 2173.
- [11] B. Felice, M. P. Prabhakaran, A. P. Rodriguez, S. Ramakrishna, *Mater. Sci. Eng., C* **2014**, 41, 178.
- [12] A. M. Inamuddin, A. M. Asiri, *Applications of Nanocomposite Materials in Drug Delivery*. UK: Woodhead Publishing; **2018**, p. 1.
- [13] P. Jana, M. Shyam, S. Singh, V. Jayaprakash, A. Dev, *Eur. Polym. J.* **2021**, 142, 110155.
- [14] X. Tong, W. Pan, T. Su, M. Zhang, W. Dong, X. Qi, *React. Funct. Polym.* **2020**, 148, 104501.

- [15] M. Sheikhpour, L. Barani, A. Kasaeian, *J. Controlled Release* **2017**, 253, 97.
- [16] A. M. Vargason, A. C. Anselmo, S. Mitragotri, *Nat. Biomed. Eng.* **2021**, 5, 951.
- [17] A. L. Yarin, B. Pourdeyhimi, S. Ramakrishna, *Fundamentals and Applications of Micro and Nanofibers*. UK: Cambridge University Press; **2013**, p. 1.
- [18] Y. Zhang, S. Sinha-Ray, A. L. Yarin, *J. Mater. Chem.* **2011**, 21, 8269.
- [19] Y. Zhang, A. L. Yarin, *J. Mater. Chem.* **2009**, 19, 4732.
- [20] J. K. Patra, G. Das, L. F. Fraceto, E. V. R. Campos, M. D. P. Rodriguez-Torres, L. S. Acosta-Torres, L. A. Diaz-Torres, R. Grillo, M. K. Swamy, S. Sharma, S. Habtemariam, H. S. Shin, *J. Nanobiotechnol.* **2018**, 16, 1.
- [21] Y. Wang, J. Yan, N. Wen, H. Xiong, S. Cai, Q. He, Y. Hu, D. Peng, Z. Liu, Y. Liu, *Biomaterials* **2020**, 230, 119619.
- [22] S. Mura, J. Nicolas, P. Couvreur, *Nat. Mater.* **2013**, 12, 991.
- [23] A. Liguori, S. Pandini, C. Rinoldi, N. Zaccheroni, F. Pierini, M. L. Focarete, C. Gualandi, *Macromol. Rapid Commun.* **2022**, 43, 2100694. <https://doi.org/10.1002/MARC.202100694>
- [24] G. Liu, W. Liu, C. M. Dong, *Polym. Chem.* **2013**, 4, 3431.
- [25] B. Sana, A. Finne-Wistrand, D. Pappalardo, *Mater. Today Chem.* **2022**, 25, 100963.
- [26] H. Chu, J. Zhao, Y. Mi, Z. Di, L. Li, *Nat. Commun.* **2019**, 10, 1.
- [27] A. Tomitaka, H. Arami, A. Ahmadvand, N. Pala, A. J. McGoron, Y. Takemura, M. Febo, M. Nair, *Sci. Rep.* **2020**, 10, 1.
- [28] P. Nakielski, S. Pawłowska, C. Rinoldi, Y. Ziai, L. de Sio, O. Urbanek, K. Zembrzycki, M. Pruchniewski, M. Lanzi, E. Salatelli, A. Calogero, T. A. Kowalewski, A. L. Yarin, F. Pierini, *ACS Appl. Mater. Interfaces* **2020**, 12, 54328.
- [29] A. Guglielmelli, F. Pierini, N. Tabiryan, C. Umeton, T. J. Bunning, L. de Sio, *Adv. Photonics Res.* **2021**, 2, 2000198.
- [30] N. Sarfraz, I. Khan, *Chem. – Asian J.* **2021**, 16, 720.
- [31] B. Singh, N. Shukla, J. Kim, K. Kim, M. H. Park, *Pharmaceutics* **2021**, 13, 1319.
- [32] F. Pierini, A. Guglielmelli, O. Urbanek, P. Nakielski, L. Pezzi, R. Buda, M. Lanzi, T. A. Kowalewski, L. de Sio, *Adv. Opt. Mater.* **2020**, 8, 20000324. <https://doi.org/10.1002/ADOM.202000324>
- [33] S. Asadi, L. Bianchi, M. de Landro, S. Korganbayev, E. Schena, P. Saccomandi, *J. Biophotonics* **2021**, 14, e202000161.
- [34] I. Capek, *Adv. Colloid Interface Sci.* **2017**, 249, 386.
- [35] H. M. Ibrahim, A. Klingner, *Polym. Test.* **2020**, 90, 106647.
- [36] M. Badmus, J. Liu, N. Wang, N. Radacsi, Y. Zhao, *Nano Mater. Sci.* **2021**, 3, 213.
- [37] J. Yoon, H. S. Yang, B. S. Lee, W. R. Yu, *Adv. Mater.* **2018**, 30, 1704765.
- [38] M. Hou, X. Y. Zhao, C. Yang, Z. Q. Xue, H. Y. Chen, J. Vac Sci, B. Zaicheng Sun, E. Zussman, A. L. Yarin, J. H. Wendorff, A. Greiner, *Adv. Mater.* **2003**, 15, 1929.
- [39] D. Han, A. J. Steckl, *ChemPlusChem* **2019**, 84, 1453.
- [40] S. Pawłowska, C. Rinoldi, P. Nakielski, Y. Ziai, O. Urbanek, X. Li, T. A. Kowalewski, B. Ding, F. Pierini, *Adv. Mater. Interfaces* **2020**, 7, 2000247.
- [41] A. L. Yarin, M. W. Lee, S. An, S. S. Yoon, *Self-Healing Nano-textured Vascular Engineering Materials*. Switzerland: Springer Nature; **2019**, p. 105. <https://doi.org/10.1007/978-3-030-05267-6>
- [42] D. N. Nguyen, C. Clasen, G. van den Mooter, *J. Pharm. Sci.* **2016**, 105, 2601.
- [43] N. Bock, T. R. Dargaville, M. A. Woodruff, *Prog. Polym. Sci.* **2012**, 37, 1510.
- [44] S. Sett, M. W. Lee, M. Weith, B. Pourdeyhimi, A. L. Yarin, *J. Mater. Chem. B* **2015**, 10, 2147.
- [45] W. Ren, X. Yu, L. Chen, T. Shi, T. Bou-Akl, D. C. Markel, *J. Biomater. Appl.* **2022**, 37, 712.
- [46] E. García-Millán, M. Quintáns-Carballo, F. J. Otero-Espinar, *Data Brief* **2017**, 15, 133.
- [47] F. Reguieg, L. Ricci, N. Bouyacoub, M. Belbachir, M. Bertoldo, *Polym. Bull.* **2020**, 77, 929.
- [48] W. Chen, A. Palazzo, W. E. Hennink, R. J. Kok, *Mol. Pharmaceutics* **2017**, 14, 459.
- [49] P. Nakielski, C. Rinoldi, M. Pruchniewski, S. Pawłowska, M. Gazińska, B. Strojny, D. Rybak, K. Jezierska-Woźniak, O. Urbanek, P. Denis, E. Sinderewicz, W. Czelejewska, J. Staszkiwicz-Chodor, M. Grodzik, Y. Ziai, M. Barczewska, W. Maksymowicz, F. Pierini, *Small* **2022**, 18, 2104971. <https://doi.org/10.1002/sml.202104971>
- [50] C. Rinoldi, E. Kijeńska, A. Chlanda, E. Choinska, N. Khenoussi, A. Tamayol, A. Khademhosseini, W. Swieszkowski, *J. Mater. Chem. B* **2018**, 6, 3116.
- [51] M. Khodadadi, S. Alijani, M. Montazeri, N. Esmaeilzadeh, S. Sadeghi-Soureh, Y. Pilehvar-Soltanahmadi, *J. Biomed. Mater. Res. A* **2020**, 108, 1444.

## SUPPORTING INFORMATION

Additional supporting information can be found online in the Supporting Information section at the end of this article.

**How to cite this article:** M. A. Haghighat Bayan, Y. J. Dias, C. Rinoldi, P. Nakielski, D. Rybak, Y. B. Truong, A. L. Yarin, F. Pierini, *J. Polym. Sci.* **2023**, 61(7), 521. <https://doi.org/10.1002/pol.20220747>